Available online at www.sciencedirect.com

Manufacturing Letters

Manufacturing Letters 33 (2022) 644–655

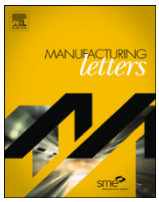

50th SME North American Manufacturing Research Conference (NAMRC 50, 2022)

3D Printing of Anisotropic Multimaterial Structures using Acoustic Streaming-assisted Two-Photon Polymerization

Ketki M. Lichade[a], Yayue Pan[a,]*

[a]Department of Mechanical and Industrial Engineering, University of Illinois at Chicago, Chicago, Illinois 60607, United States

*Corresponding author. Tel.: +0-312-996-8777; fax: +0-312-413-0447. *E-mail address:* yayuepan@uic.edu

Abstract

Recently, many studies have investigated anisotropic multimaterial structures for their potential in various applications, thanks to their tunable anisotropic physical properties. A significant challenge in these product innovations is the limited choices of manufacturing technologies for fabricating the desired anisotropic multimaterial structures with precise topological and chemical composition control. This study reports a new manufacturing method, Acoustic-Streaming-assisted Two-Photon Polymerization (AS-TPP), for fabricating anisotropic multimaterial structures through integrating layer-by-layer printing and acoustic-streaming-assisted particle patterning at a nano- and micro- scale. To study the effectiveness of this method, a set of structures with different topology and material compositions is fabricated using the conventional TPP technique and this novel AS-TPP technique. The scanning electron microscope (SEM) and energy-dispersive X-ray spectroscopy (EDS) analysis of the fabricated samples validated the accuracy of the AS-TPP process in the geometry and material composition control. Experimental results validated the manufacturing capability of the novel AS-TPP process in terms of material patterning, surface structuring, and anisotropy production. To demonstrate possible applications, the anisotropic wettability and water collection capability of the printed samples were measured and compared. The water collection efficiency of the anisotropic multimaterial structure with groove surface fabricated by AS-TPP was three times higher than that of the isotropic single-material structure with flat smooth surface. This work implied the great potential of the AS-TPP technique for the productions of materials or devices with advanced shape and material designs for various applications such as microfluidics, optics, functional surface coating, cell screening, and biomedical devices.

Keywords: Acoustic Streaming, Two-Photon Polymerization, Anisotropic Structure, Multi-material Additive Manufacturing, Fog Harvesting, Anisotropic Wetting

1. Introduction

1.1 Literature review of anisotropic structures

Anisotropic structures (AS) have received extensive attention over flat isotropic structures (IS) due to their remarkable anisotropic physical properties, including wetting, adhesion, and directional cell growth [1]. Anisotropic structures found on many biological species consist of micro/nanostructures, including bent, inclined, zigzag, and helical pillars, which have been recently reviewed by Tawfick *et al.* [2]. For instance, feet of wall climbing insects and reptiles such as geckos, lizards, and spiders, consisting of arrays of angled branching hierarchical fibers with spatula-shaped tips, enable anisotropic adhesive properties on vertical walls [3]. Butterfly wings show directional adhesive properties due to the direction-dependent arrangement of overlapped nano-stripes. This unique topological anisotropy causes droplets to easily roll off along the outward radial direction, causing butterfly wings to remain dry during rain [4]. Similarly, the grooved patterns found on the surfaces of many plants, including grass and rice leaf, have displayed unique directional water transport mechanisms [5].

Inspired by nature, biomimetic anisotropic structures have been designed and fabricated using chemical and physical approaches, including interference lithography [6], replica molding [7], laser processing [8], and chemical etching [9]. For

instance, Parness *et al.* [7] fabricated adhesive surfaces with gecko-inspired wedge-shaped microstructures using dual exposure lithographic molding. The fabricated structure showed remarkable directional adhesive properties even after 30000 cycles. Inspired by various biological interfaces, Wang *et al.* [10] manufactured composite color patches with an anisotropic surface adhesion for tissue engineering applications. Moreover, Lu *et al.* [8] fabricated a rice leaf-inspired microgrooved surface by tuning the pulse energy of the femtosecond laser. They found that the water collection efficiency of the anisotropic surface was four times higher than the isotropic surface. Reported work in these and other references, e.g., [11–14], demonstrated that anisotropy resulting from bioinspired topology and arrangement of micro/nanostructures could enable anisotropic properties important or even necessary for a wide range of applications.

To further enhance these anisotropic properties, an approach is to combine surface topology and materials with chemical contrast, first found by Parker *et al.* [15]. The combination of surface topology and chemical contrast observed in nature has inspired many studies of anisotropic materials [16–19]. For instance, Zong *et al.* [18] observed higher anisotropic wetting on the grooved surface composed of silicon dioxide (CA: 0°) and SU8 (CA: 63°) compared to the grooved surface composed of silicon dioxide alone. Yang *et al.* [19] fabricated various hydrophobic-hydrophilic patterns using electrochemical etching, showing 92.7% higher water collection efficiency compared to that of the flat hydrophilic surface. Li *et al.* [20] studied the effect of laser patterned anisotropic multimaterial grooved surface on cell adhesion. It was observed that the cells cultured on a patterned surface showed better alignment than on a flat surface. In addition to line patterns, anisotropic multimaterial surfaces were further designed and fabricated with complicated shapes, such as topology mimicking leaf veins [21,22].

1.2 Challenges in manufacturing of anisotropic structures

Despite the remarkable achievements in the design and development of anisotropic structures, the majority of the manufacturing processes in these work involve complicated processing steps, such as lithography in combination with thin-film technology and surface modification, followed by pattern removal by etching or laser ablation [1]. In addition to long fabrication time and generation of wastes [23], the existing surface structuring technologies can only process a single material and have limited capability to pattern multi-materials at micro/nano-scale. As a result, the single-material surface patterns fabricated using most surface modification techniques have limited durability and robustness, i.e., can only be effective for several days or cycles [24]. It is challenging to maintain the long-term stability and durability of the engineered wettability patterns under severe external forces or harsh environmental conditions.

In contrast to these traditional indirect manufacturing processes, Additive Manufacturing (AM) techniques provide the direct manufacturing ability to orient and pattern the filling material with very different chemical structures and physical properties (e.g., hydrophilic particles) on the base material (e.g., hydrophobic polymer) with simultaneous control on shape and material composition. Various AM processes, such as inkjet printing [25,26] and Fused Deposition Modeling (FDM) [27], have been utilized to fabricate anisotropic multimaterial surfaces for a variety of applications.

The multimaterial AM techniques are facile to fabricate anisotropic multimaterial components with varied surface structures on varied substrates; however, the resolution of fabricated components is usually limited to a few hundreds of micrometers [28]. Since the accuracy and precision of the surface patterns and material distributions play a vital role in the property anisotropy, the development of a high-resolution multimaterial additive manufacturing method is necessary to explore the full potential of anisotropic multimaterial surfaces.

The Two-Photon Polymerization (TPP) process has found to be a high-resolution approach for fabricating three-dimensional (3D) structures (i.e., resolution of a few hundreds of nanometers or even sub-100 nm), by selectively polymerizing photosensitive liquid resin in a voxel-by-voxel and layer-by-layer manner. The high manufacturing resolution and direct printing mechanism implies the potential for creating anisotropic surfaces with precise control over the material contrast and micro- or even nano-scale shape details [1].

However, according to the author's best knowledge, the anisotropic properties achieved by samples printed by the TPP process have mainly relied on constructing surface structures rather than material contrasts, owing to the limited choices of printable materials and limited capability in manipulating multiple materials in a small droplet [29–31]. To address this challenge, one way is to integrate functional nanomaterials to modify the chemical composition of the conventional TPP resin. For instance, Lakhotia *et al.* [32] found that by mixing magnetic nanoparticles (MNPs) and increasing its concentration from 0.05 wt% to 0.2 wt%, the printed polyethersulfone (PES) membrane can be changed from hydrophobic to hydrophilic. A big challenge in curing nanoparticle-polymer composite liquid with the TPP process is that nanoparticles move upon laser irradiation due to the photothermal effect, leading to structural defects and bubbles during the printing [33]. Furthermore, although homogeneous composites have been successfully printed using two-photon polymerization of composite liquids, it is very difficult to manipulate and pattern particles in the liquid droplet during TPP printing to fabricate anisotropic parts with chemical contrasts.

1.3 Research objectives and research plan

In our previous work, we have proposed an approach to eliminate the photothermal effect by balancing the laser power of the polymerization threshold of photoresist and photothermal instability of the nanoparticles [33]. Based on this approach, we developed a novel method named Acoustic Streaming-assisted

Two-Photon Polymerization (AS-TPP) process [34]. Here, high-resolution anisotropic multimaterial structures with groove surface can be printed through two-photon polymerization by first printing layers with micro-sized grooves, then driving nanoparticles into the pure polymer groove areas via acoustic-field assisted microcirculation and lastly, selectively curing the multi-material groove area to lock particle patterns in the polymer.

The AS-TPP process can bring many benefits over conventional manufacturing processes. For instance, varied substrates can be selected for different applications, including conductive silicone, flexible PET, or glass substrate, and function as an integral part of the final product. In addition, different with magnetic patterning or electric-field-assisted patterning which requires particles to be magnetic or electrically conductive, acoustic patterning has no requirement on physical properties of the particles and hence work with a wide range of particles which can contribute to various functionalities, such as electrical conductivity, cell adhesion, chemical sensitivity, and mechanical strength. Such large flexibilities in substrate selection and particle selection are significant for enabling a wide range of applications, including biological sensing, microelectronics, microfluidics, and optics [35].

Considering these advantages, in this work, we report the design, fabrication, and potential applications of bioinspired anisotropic multimaterial structures fabricated using the novel AS-TPP process. The rest of this paper is organized as follows. Section 2 presents the design of a bioinspired anisotropic structure characterized by both high chemical contrast and groove surface structures. Section 3 describes the experimental details, including manufacturing setup and processes. Manufacturing challenges, solutions, and manufacturing results are discussed in Section 4. Potential applications are also examined and discussed in Section 4. Lastly, conclusions are drawn in Section 5.

2. Bioinspired Design of Anisotropic Multimaterial Surfaces

The anisotropic behavior of many natural spices is governed by the combination of surface topology and chemical contrast. For instance, the Namib beetle back has been widely studied for its unique water collection mechanism [36]. The Namib beetle back consists of hydrophilic bumps with flat hydrophobic surroundings. Due to the surface energy gradient, the water carried by fog gets collected on the hydrophilic bumps, as shown in **Fig. 1a**. Once the droplet becomes large enough, it rolls down towards the beetle's mouth through the hydrophobic area. This surface energy gradient caused by the chemical contrast of the hydrophilic and hydrophobic materials influences the water collection and transportation mechanism [36]. Although these features have enabled fast water collection, they lack directional transport of collected water. In another example, the grooves on rice leaf create a significant difference in water contact angle along the parallel and perpendicular directions [5]. With this unique topology, the water rolls down, enabling the continuous directional water supply to the root, as shown in **Fig. 1b**.

Inspired by these biological features, our surface design proposed in this study consists of hydrophilic grooves surrounded by a hydrophobic plateau for continuous water collection and directional transportation of water, as illustrated in **Fig. 1c.** On this surface, the fog gets deposited on the hydrophobic polymer region (process 1 in Fig.1c), and the surface energy gradient induced by the wettability contrast can act as a driving force to move these water droplets into the hydrophilic composite groove area (process 2 in Fig.1c). In addition, the Laplace pressure gradient induced by the groove topology can contribute to the directional transportation of collected droplets (process 3 in Fig.1c).

In this work, an inverse tapered groove shape was chosen over the conventional triangle and rectangular shapes because of its excellent nanoparticle trapping [37] and higher anisotropic wetting behavior [38]. The CAD model and geometric parameters of the design proposed in this study are shown in **Fig 2a**. Here, W_t, W_b, and H are the top width, bottom

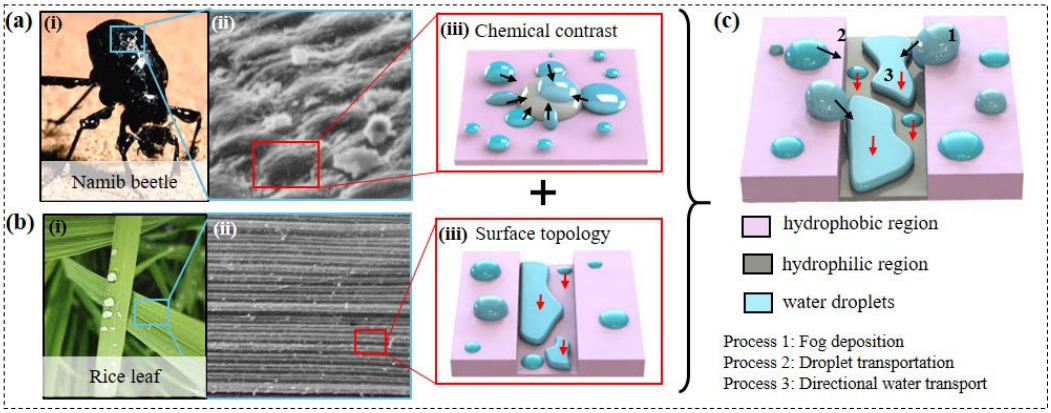

Fig. 1 Schematic of the fog-harvesting process on (a) beetle back surface: **(i)** optical image of an Namib-dessert beetle; **(ii)** microscopic image of beetle back features; **(iii)** illustration of water collection mechanism (black arrow: surface energy gradient) [52]; **(b)** rice leaf surface: **(i)** optical image of a rice leaf; **(ii)** microscopic image of microgroove structures on the rice leaf; **(iii)** illustration of water collection mechanism (red arrow: Laplace pressure gradient); **(c)** the proposed surface consisting of hydrophilic microgroove patterns surrounded by hydrophobic plateau for enhanced water collection (black arrow showing the surface energy gradient and red arrow showing the Laplace pressure gradient).

Table 1. Specifications of the four groups of samples.

Sample	Surface feature		Fabrication Process	Dimensions (μm)				
	Topography	Chemistry		H	D	W_t	W_b	L
S_{pf}	Flat, smooth	Pure polymer	TPP	5	NA	NA	NA	2000
S_{cf}	Flat, smooth	Composite	TPP	5	NA	NA	NA	2000
S_{pg}	Microgrooves	Pure polymer plateau and groove	TPP	5	2	10	12	2000
S_{cg}	Microgrooves	Pure polymer plateau and composite groove	AS-TPP	5	2	10	12	2000

Note: ''p'' in the sample names denotes pure polymer whereas ''c'' for composite material; ''f'' denotes flat smooth surface whereas ''g'' for the grooved surface.

width, and depth of the groove area without nanoparticle trapping. D is the depth of the groove area after nanoparticle trapping and curing. The total length of the surface is L. Inspired by the beetle back microstructure, the ratio of hydrophobic pure polymer area and hydrophilic composite groove area was designed to be 2:1 [15]. Furthermore, the groove dimensions were selected in such a way that the ratio H/W_t is 0.5 and $W_b > W_t$, which was found to be the optimum design for efficient particle trapping [40,41].

For comparison, four components with different surface topology and material composition were designed and fabricated, namely flat pure polymer surface (S_{pf}), flat composite surface (S_{cf}), pure polymer surface with polymer groove structure (S_{pg}), and pure polymer surface with composite groove structure (S_{cg}). The schematic of these four surface designs is presented in **Figs. 2b-e**. The design parameters and specifications of each surface design are summarized in **Table 1**. Although S_{pg} and S_{cg} have identical geometry, sample S_{cg} is chemically heterogeneous, characterized by a high material contrast between the groove and plateau areas. Samples S_{pf} and S_{cf} have no grooves and are chemically homogeneous but different in material composition as indicated by the subscripts.

3. AS-TPP Manufacturing of the Bio-Inspired Multi-Material Anisotropic Structures

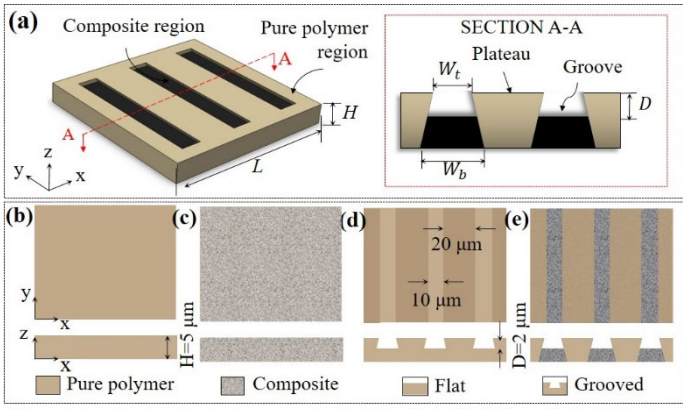

Fig. 2 Schematic of (a) the proposed anisotropic multimaterial surface model showing design parameters; **(b)** flat smooth pure polymer surface (S_{pf}); **(c)** flat smooth composite surface (S_{cf}); **(d)** grooved pure polymer surface (S_{pg}); **(e)** grooved surface with pure polymer plateau and composite grooves (S_{cg}) with design details shown in (a).

Table 2. Properties of various nanoparticles used in this study

Specification	Silver	Diamond	Copper	Iron oxide
Size (nm)	<100	<100	60-80	20-30
Density (g/cm3)	10.49	-	8.94	0.84

3.1 Material preparation

IP-L 780 photoresist (Nanoscribe GmbH, Eggenstein-Leopoldshafen, Germany) was used as purchased to fabricate the hydrophobic pure polymer region in our designs. In this study, to identify proper nanoparticles for fabricating the hydrophilic composite region in our designs, four types of nanoparticles were tested, including iron oxide (Sigma-Aldrich, St. Louis, MO), copper (Sigma-Aldrich, St. Louis, MO), silver (Sigma-Aldrich, St. Louis, MO), and diamond nanoparticles (Electron Microscopy Sciences, Hatfield, PA). Details of these nanoparticles are listed in **Table 2**.

The hydrophilic composite liquid was prepared using the method developed in our previous work [34], as illustrated in **Fig. 3.** First, nanoparticles were added to isopropyl alcohol (IPA) (Sigma-Aldrich, St. Louis, MO), and the solution underwent ultrasonic agitation (U.S. Solid, Cleveland, OH) for 2 minutes to break large nanoparticle aggregates. Excess IPA was removed using centrifugation followed by evaporation. For magnetic nanoparticles, a decantation process was utilized to separate excess IPA. The remnant nanoparticles were dispersed in IP-L photoresists with 1 wt% Irgacure 369 (Sigma-Aldrich, St. Louis, MO). The mixture was stirred for 24 hours to obtain a homogeneous distribution. The solution was then purified using centrifugation to remove large nanoparticle aggregates from the composite mixture; thus, the final composite has a real filler concentration lower than the original mixture. Before printing, 20 wt% thiol molecules were added into the mixture to prevent the photothermal effect [33].

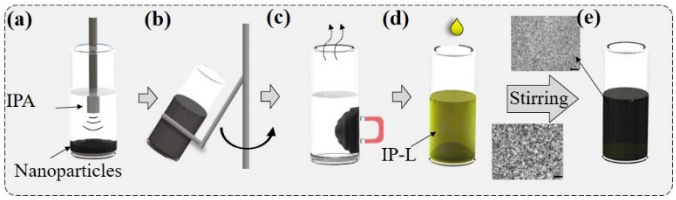

Fig. 3 Particle-polymer composite liquid preparation for AS-TPP process: (a) ultrasonic agitation; **(b)** centrifugation; **(c)** decantation and IPA evaporation; **(d)** addition of IP-L; **(e)** composite material.

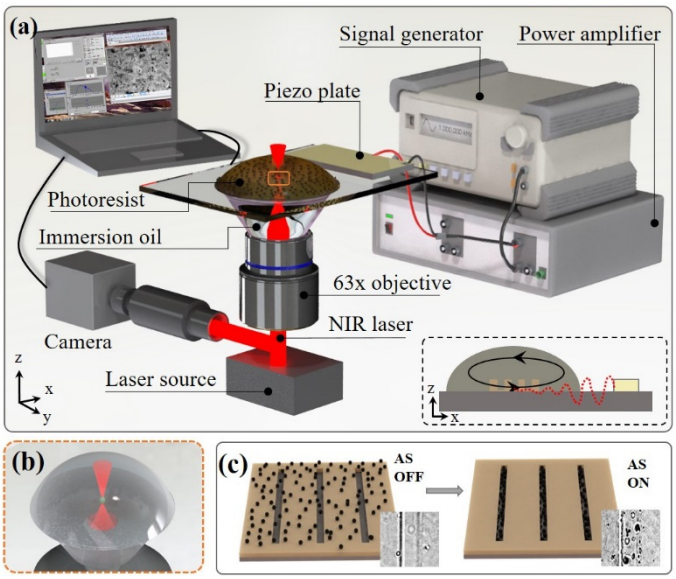

Fig. 4 The proposed AS-TPP process: (a) Schematic of the AS-TPP setup (inset: schematic of acoustic streaming assisted microcirculation within liquid droplet); **(b)** a laser beam focused into the liquid resin; **(c)** patterning of NPs using acoustic streaming (inset: phase-contrast images of a single groove before and after NP trapping during the AS-TPP process).

3.2 Overview of the AS-TPP manufacturing system

A rectangular-shaped piezoelectric plate (L: 20 mm, W: 15 mm, H: 1 mm) (Steiner & Martins, Inc., Davenport, FL) was attached on the top of the polyethylene terephthalate (PET) film (Sigma-Aldrich, St. Louis, MO) (film thickness: ~127 µm). The acoustic signal was generated by a function generator (RIGOL Technologies Inc., Beijing, China) and further amplified (TEGAM Inc., Geneva, OH) to actuate the acoustic streaming (AS).

A commercial Two-Photon Polymerization (TPP) machine (Nanoscribe GmbH, Eggenstein-Leopoldshafen, Germany) was retrofitted by integrating the acoustic setup, as illustrated in **Fig. 4a**. In the system, a femtosecond pulsed laser emitting at 780 nm, with a pulse width of 100 fs and a repetition rate of 80 MHz, was used as the laser source. The Galvo mode was utilized for scanning in the x and y direction, and the piezo mode was used for z-direction movement. Based on the findings in our previous work [33], the laser power was set at 22% and 17% for curing the pure polymer and composite material, respectively. The slicing and hatching distances for all printing jobs were set to be 0.4 µm and 0.3 µm, respectively. The laser beam was focused into the liquid resin using an oil immersion objective lens (63x, N.A.= 1.4), as illustrated in **Fig. 4b**.

Upon actuation of the acoustic field using the piezoelectric plate, nanoparticles start to stream within the composite droplet, along a direction perpendicular to the microgroove long axis, which results in nanoparticle trapping inside the previously cured groove area, as illustrated in **Fig. 4c**. However, at low concentrations, the number of nanoparticles trapped inside the groove space was almost negligible. Although particles enter into the groove space during acoustic streaming, they quickly escape to the outside flow since they are unrestrained by the nanoparticles in the main flow. On the other side, a higher concentration of NPs in the main flow adds more particle interaction; as a result, it provides a larger restriction to particle escape [41]. The particle trapping during AS-assisted microcirculation was monitored using a microscope (Axio Observer Z1, ZEISS, Oberkochen, Germany). Experiments showed that a nanoparticle concentration of 1.5 wt% or higher

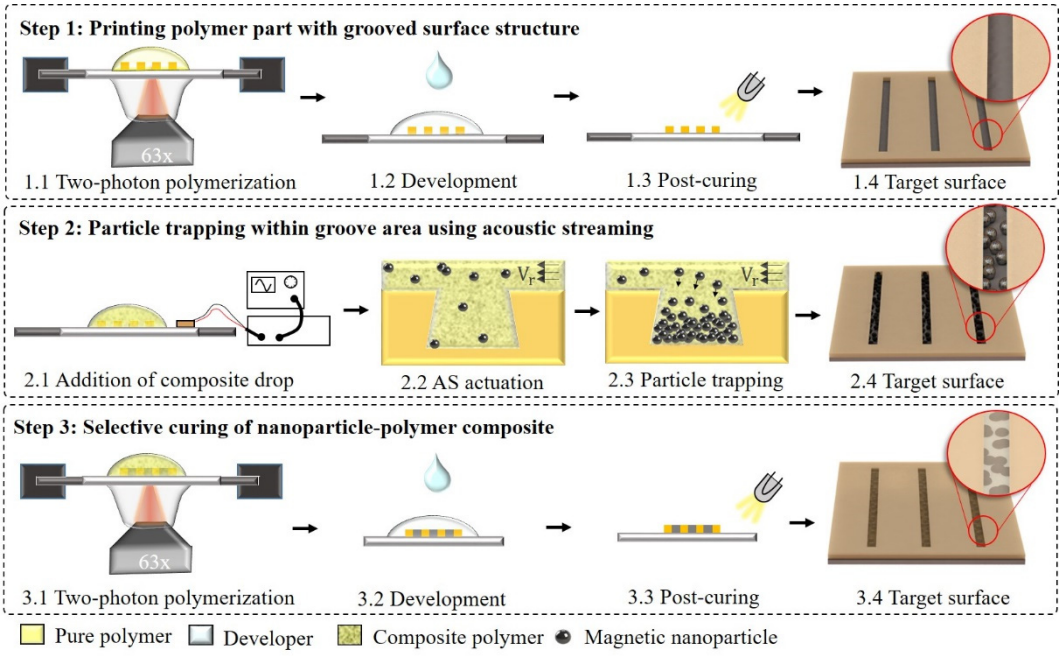

Fig. 5 Fabrication procedure using conventional TPP process and the proposed AS-TPP process.

was found effective for particle trapping. Using this setup and the AS-TPP process, the models designed in Section 2 were fabricated with multiple replicates and experimentally characterized as described below.

3.3 Manufacturing process

As shown in **Fig. 5**, the AS-TPP fabrication process involves three main steps: (Step 1 in Fig.5) curing the pure polymer region of the layer using conventional TPP process while leaving the particle-filled region empty with an inverse tapered groove design, (Step 2 in Fig.5) Acoustic-streaming-assisted microcirculation and trapping of nanoparticles in the groove area, and (Step 3 in Fig.5) curing the particle-polymer composite in the groove area using laser irradiation. To be more specific, following the conventional TPP process, a composite drop was placed onto the groove area of the printed polymer part (step 2.1 in Fig.5), and the acoustic field was actuated at the resonance frequency and input voltage of 1.1 MHz and 5V (step 2.2 in Fig.5), respectively. Upon actuation, nanoparticles start streaming within the liquid droplet with a velocity of 0.151 µm/s, flowing toward the grooves and being trapped inside the grooves (step 2.3 in Fig.5). After successfully trapping nanoparticles, the TPP process continued to selectively cure the particle-polymer composite inside the grooves based on the voxel location (step 3.1 in Fig. 5). This three-step procedure was repeated until the last layer was printed. Then, the uncured resin was washed away by immersing the part in SU-8 for 9 min and IPA for 2 min (step 3.2 in Fig.5), followed by air-drying and post-curing for 45s (step 3.3 in Fig.5).

3.4 Manufacturing challenges and process optimization

The first challenge is related to the printing size and printing stability. With the Nanoscribe machine, the maximum area that can be printed in Galvo mode is 140 × 140 µm^2. Printing a larger area, such as the 2 × 2 mm^2 in step 1, requires stitching of multiple 140 × 140 µm^2 blocks. The splitting of the 2 × 2 mm^2 section of the proposed surface into small blocks is shown in **Fig. 6a**, where each small area corresponds to the 140 × 140 µm^2 block. For each small area, the Nanoscribe machine first finds the interface between the substrate and the resin (**Fig. 6b**), then prints the 140 × 140 µm^2 units one by one using the Galvo mode. After printing one 140 × 140 µm^2 unit, the piezo stage moves to the center of the next unit to print the next unit, and the process continues till the entire structure is printed. This procedure has been successfully implemented in printing polymer components on glass substrates. However, the PET film was selected as the substrate (**Fig. 6c**) in this study because its flexibility is favorable for acoustic streaming, but the flexibility of PET film makes the interface identification process much more challenging than the glass substrate, leading to failure in finding a stable interface during step 1 (**Fig. 6d)** and hence printing failure.

To address this issue, the thin PET film was attached to a rigid glass substrate, and the PET-glass combination was used as the liquid droplet support, as shown in **Fig. 6e**. It is worthwhile to mention that there is always an inevitable air gap between the PET film and the glass substrate. Since the objective lens uses the difference between refractive indices to identify the interface for printing, the air gap (refractive index: 1) between the PET film (refractive index: 1.57) and the glass plate (refractive index: 1.52) interfered with the PET-liquid interface identification process. As shown in **Fig 6f**, the system would detect two interface signals, i.e., PET-air interface and air-glass interface. As a result, the laser irradiation would fail to focus on the right plane for printing. To overcome the challenge in detecting the correct printing surface, a small drop of IPA liquid was added between the glass and PET film to avoid creating any air gap between them. The schematic

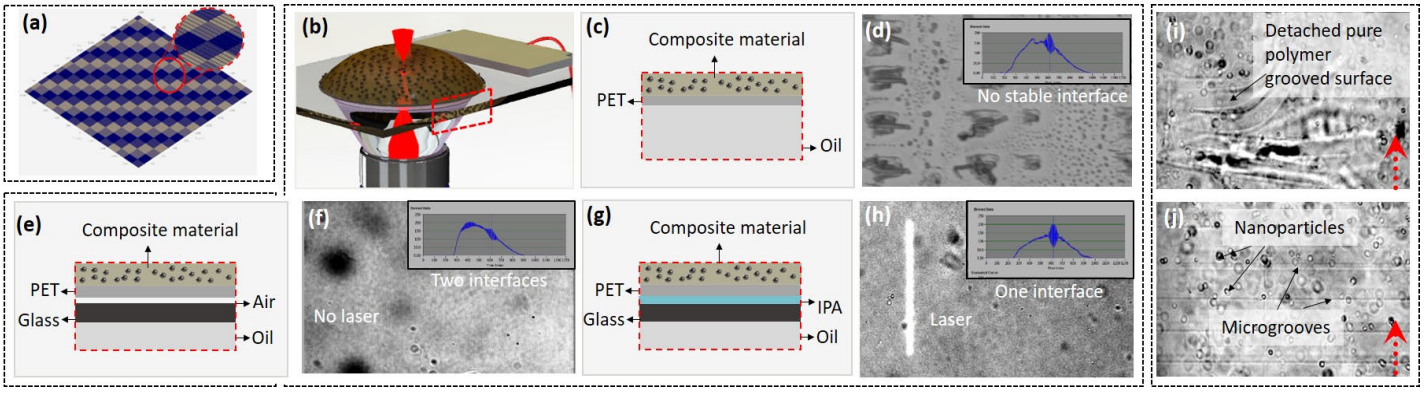

Fig. 6 AS-TPP manufacturing challenges and the corresponding approaches adopted in the three steps: challenge in step 1: (a) isometric view of 2 × 2 mm^2 surface showing the stitching of multiple blocks during printing; **(b)** challenge of the liquid-substrate interface identification in the AS-TPP setup; **(c)** schematics of the PET film substrate; **(d)** surface printing failed in step 1 due to the deformation of PET film; **(e)** schematics of the modified PET-Glass substrate to eliminate deformation; **(f)** incorrect interface finding due to the undesired air gap; **(g)** schematics of the modified PET-IPA-Glass substrate for tuning refractive index; **(h)** accurate interface was found after adding IPA**; Challenge in step 2: (i)** in-situ microscopic phase-contrast image of the printing area showing that the pure polymer layer printed in step 1 detached from the substrate during the acoustic streaming process and thus printing failed in step 2; **(j)** in-situ microscopic phase-contrast image of the printing area showing that polymer layer stayed attached during the whole acoustic streaming process in step 2 (red arrow indicates the direction of acoustic-streaming-assisted particle flow).

of the modified substrate is shown in **Fig. 6g**. Since the IPA refractive index is 1.377, which is very close to those of the glass (1.52) and the PET film (1.57), it could enable the correct interface signal on the PET-liquid interface (**Fig. 6h**), and hence allow for laser irradiation on the correct plane for two-photon curing in step 1.

During step 2, the crucial issue encountered was that the pure polymer layer previously printed in step 1 often detached from the PET substrate and floated during the acoustic streaming process, as shown in **Fig. 6i**. This was more likely caused by the stress generated due to the particle flow during acoustic streaming within the liquid droplet. To improve the adhesion of the printed part to the PET substrate and avoid detachment in step 2, one approach is to increase the number of base layers. However, this method is not desired in our study because it could create a discrepancy between the height of the designed and the printed structure. Therefore, to ensure successful attachment, the post-curing (i.e., step 1.3 in Fig. 5) time for the pure polymer part was carefully tuned in a way that the polymer can be fully cured yet would not create warpage, and 10s was found to be appropriate. This method achieved successful attachment throughout the acoustic streaming process (i.e., step 2.2 in Fig. 5), as shown in **Fig. 6j**. The red arrow indicated the direction of nanoparticle flow.

4. Results and Discussion

4.1 Fabrication and morphological characterization of proposed models

Using manufacturing processes described in sections 3.3.1 and 3.3.2, the four models were fabricated using feedstock prepared by mixing 1.5 wt% of black iron oxide particles with the liquid IP-L resin as described in section 3.1. **Figures 7a-d** show phase-contrast images during printing, where black color is iron oxide nanoparticles, and gray background is IP-L resin. To validate the printing accuracy of the AS-TPP process, the printed samples were observed under a scanning electron microscope (JSM-IT500HR FESEM, JEOL, Tokyo, Japan) using its high vacuum mode. The spot size and the accelerating voltage of the SEM were 4.0 and 5.0 kV, respectively. Prior to SEM imaging, the samples were sputter-coated with a 6 nm platinum layer to avoid charging. The weight percentage and distribution of iron oxide nanoparticles were measured by energy-dispersive X-ray spectrometry (EDS). The working distance and accelerating voltage of the EDS were 10 mm and 15 kV.

Figures 7e-h show the SEM images of the four printed surfaces. The dimensions measured using SEM images agree well with the designed geometries. The EDS maps presented in **Figs. 7i-l** show the distribution of the Fe element (red color) in the four printed samples. It can be seen that Fe is distributed homogeneously in the S_{cf} sample, whereas no Fe content was observed on both S_{pf} and S_{pg} surfaces. On the other hand, Fe was highly concentrated within the groove area in the S_{cg} sample.

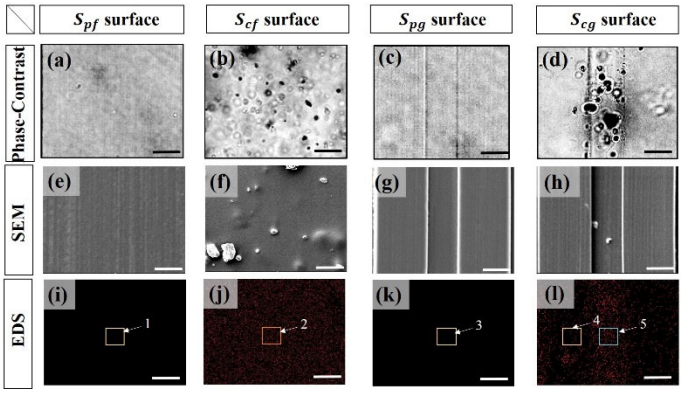

Fig. 7 Characterization of four surfaces: (a)-(d) phase-contrast images; **(e)-(h)** SEM images; **(i)-(l)** EDS maps of Fe element: red color indicates Fe element and black color indicates polymer background (Scale bar: 10 μm).

Table 3. The concentrations (wt%) of different elements in printed samples

Element	Region 1, 3, 4	Region 2	Region 5
C	68.73	73.82	65.06
O	31.25	24.2	30.16
S	0.02	0.63	1.19
Fe	0	1.35	3.59

The quantitative results of the EDS spot profiles summarized in **Table 3** indicate the difference between Fe concentrations in different regions of the printed samples. The weight percent of Fe was 3.59% in the composite region of the S_{cg} sample, but 0% and 1.35% in the pure polymer region of the S_{cg} sample and S_{cf} sample, respectively. The concentration of nanoparticles within the groove areas of the S_{cg} sample was 2.66 times of the concentration in the plateau areas, indicating successful acoustic trapping and focusing. The quantitative measurements of SEM and EDS validated that the AS-TPP process is effective in printing anisotropic multimaterial samples with concentrated nanoparticle distribution and high chemical contrast.

4.2 Water contact angle and anisotropic wettability

According to literature, larger wettability anisotropy, denoted by a larger contact angle difference Δθ between contact angles along two orthogonal directions, is desirable for self-driven water collection applications. Moreover, this anisotropy in difference between the surface energy of two materials. As shown in **Fig. 8**, a material with high surface energy leads to hydrophilicity, whereas low surface energy leads to hydrophobicity [42]. Therefore, to select a composite material with the highest surface energy difference from pure polymer, flat composite surfaces with various nanoparticles were fabricated using the TPP process. The concentration of nanoparticles in the composite mixture was 1.5 wt%. The specifications of different nanoparticles used in this experiment are summarized in **Table 2**.

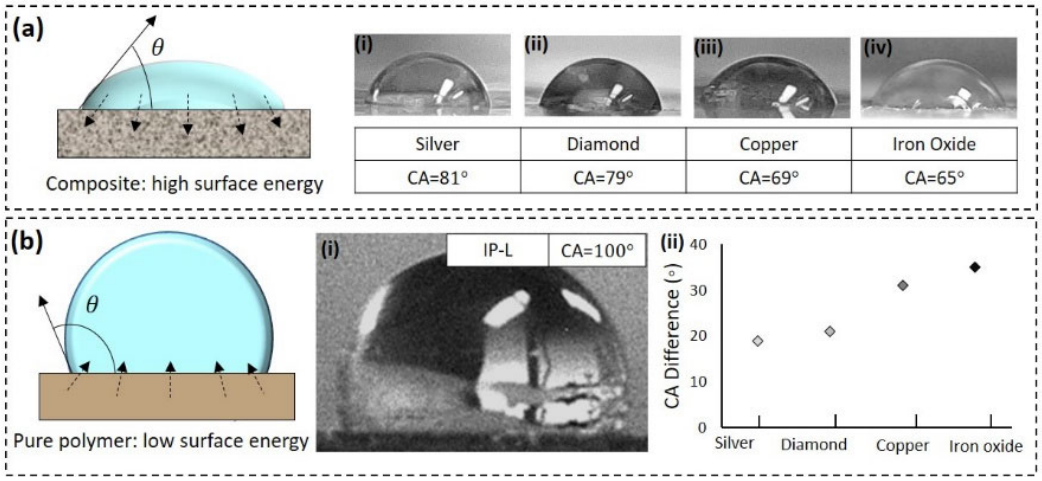

Fig. 8 (a) Schematic of water droplet demonstrating the relationship between high surface energy and wettability, optical images illustrating the contact angle of a water droplet on flat composite surface fabricated using nanoparticles including **(i)** silver, **(ii)** diamond, **(iii)** copper, **(iv)** iron oxide (MNPs); **(b)** schematic of water droplet demonstrating the relationship between low surface energy and wettability, **(i)** optical images illustrating the contact angle of a water droplet on the flat polymer surface, **(ii)** wettability difference between composite and pure polymer surfaces.

To characterize the wetting properties and anisotropies of the printed samples, contact angle measurements were performed using a sessile drop technique. Deionized water (DI) droplets of approximately 1.5 µL were carefully placed onto the sample surfaces. The water contact angle was measured using a dynamic contact angle measuring device (DCAT-25, DataPhysics Instruments, Charlotte, NC), with a range of 0-180° and measurement accuracy of 0.01°. All measurements were conducted at room temperature and a controlled humidity of 45%. The measurements were repeated 3 times for accurate results.

The contact angles of the four samples composed of different particle-polymer composite materials were measured, as shown in **Figs. 8a (i)-(iv)**. A flat composite surface with silver nanoparticles showed the highest contact angle of 81°, whereas iron oxide magnetic nanoparticles (MNPs) showed the smallest contact angle of 65°. This reduction is due to the large surface area provided by MNPs, making it the most effective for increasing the surface energy and wettability [32]. For comparison, the contact angle of a flat pure polymer surface was measured as 100° (**Fig. 8b (i)**). The difference between the contact angles of pure polymer and the composite surface was plotted in **Fig. 8b (ii)**. The composite surface composed of MNPs showed the largest difference in wettability (35°). Therefore, MNPs polymer composite was selected as the hydrophilic composite material to investigate the AS-TPP printing of the anisotropic multimaterial components and its potential applications.

To study the anisotropic wetting behavior, four components with different material composition and surface topology, including S_{pf}, S_{cf}, S_{pg}, and S_{cg}, were fabricated using IP-L polymer as a hydrophobic material and MNPs-filled IP-L polymer composite as a hydrophilic material. The specifications of these samples were the same as given in **Table 1**. The overall dimension of the printed sample was 2 mm × 2 mm × 5 µm. The difference between contact angles along a line parallel to (xz plane: $\theta_{\parallel}$) and a line perpendicular to (yz plane: $\theta_{\perp}$) the groove direction was evaluated. To observe the anisotropic behavior of the droplet, images of the top view were captured using an optical microscope (MicroVu, Windsor, CA). The optical images of these four sample surfaces and the water droplets on the four sample surfaces are shown in **Fig. 9**.

Experiment results revealed that both flat surfaces exhibited isotropic wetting. The flat pure polymer surface (S_{pf}) is hydrophobic with a water contact angle of $\theta_{\parallel} = \theta_{\perp} = 100°$, and the flat composite surface (S_{cf}) is hydrophilic with a water contact angle of $\theta_{\parallel} = \theta_{\perp} = 65°$, as shown in **Figs. 9a (i)** and **(ii)**, respectively. The top view of the water droplet on these surfaces has a circular shape of different sizes. These results indicate that there is a significant difference in the surface energy of both materials. Samples with groove surface structure exhibited anisotropic wetting behavior. On the grooved pure polymer surface (S_{pg}), the wettability behavior changed to slightly anisotropic wetting with $\theta_{\parallel} = 80°$ and $\theta_{\perp} = 64°$, as shown in **Fig. 9b (i)**. Moreover, as shown in **Fig. 9b (ii)**, the contact angle measured on sample S_{cg} along the line parallel to and the line perpendicular to the microgrooves was $\theta_{\parallel} = 96°$ and $\theta_{\perp} = 53°$. The top view of the water droplet on these surfaces has an ellipse-like shape. Owing to the existence of an energy barrier due to the microgrooves, the droplet size is shortened along the x axis on the xz plane. On the other hand, the droplet is stretched along the y axis on the yz plane since the droplet is subjected to Laplace force.

The measured contact angles and anisotropy between parallel and perpendicular directions are summarized in **Fig. 9c**. More pronounced anisotropic wetting was observed on S_{cg} ($\Delta\theta$=43°) surface compared to S_{pg} ($\Delta\theta$=17°), because the wettability contrast of composite/polymer materials in the S_{cg} further enhances the anisotropy along the perpendicular and parallel directions [18]. Our results agree well with results reported in the literature that suggested that the integration of

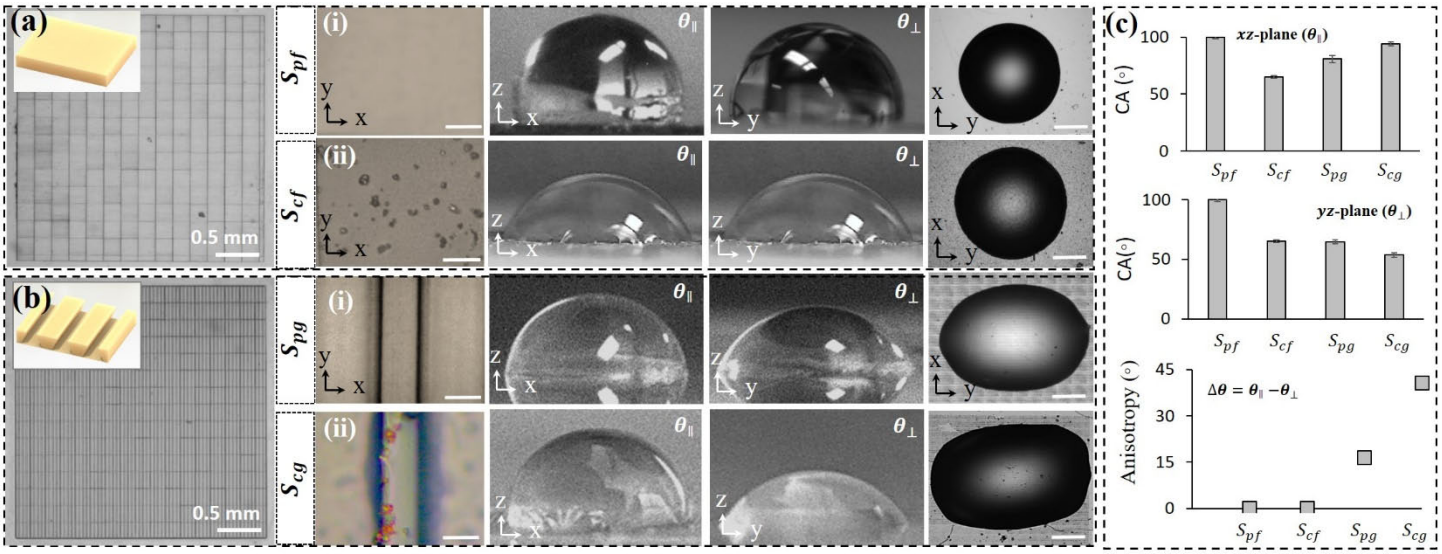

Fig. 9 Contact angle measurements: (a) optical image of a flat smooth surface printed by the TPP setup, **(a-i)** microscopic image of the printed flat polymer surface S_{pf} (Scale bar: 10 µm), side view on the xz plane, side view on the yz plane, and top view (on xy plane) of a water droplet sitting on top of the printed surface (scale bar: 250 µm), **(a-ii)** microscopic image of flat composite surface S_{cf} (scale bar: 10 µm), side view on the xz plane, side view on the yz plane, and top view (on xy plane) of a water droplet sitting on top of the printed surface (scale bar: 250 µm); **(b)** optical image of a grooved surface printed by the TPP setup using the proposed AS-TPP process, **(b-i)** microscopic image of the printed grooved polymer surface S_{pg} (scale bar: 10 µm) and views of a water droplet sitting on it (scale bar: 250 µm), **(b-ii)** microscopic image of the printed grooved polymer surface S_{cg} (scale bar: 10 µm) and views of a water droplet sitting on it (scale bar: 250 µm); **(c)** plots of contact angles on xz plane, yz plane, and differences of the contact angle ($\Delta\theta$) on these two planes (i.e., wetting anisotropy).

groove surface structure and surface chemistry contrast increases anisotropic wetting (Δθ) [43].

4.3 Fog harvesting and water collection efficiency

The fog harvesting capability and water collection efficiency of the printed films were evaluated using a homemade setup in the lab. The setup was constructed based on the previously published work [46]. The schematic and optical image of experimental setup is illustrated in **Fig. 10.** A household humidifier (Humidifying capacity: 50 mL/h – 210 mL/h, Power: 20 W) was used to simulate fog. The fog size created in this study is in the range of 1-40 µm in fog drop diameter [47], which matches well with the typical fog size found in nature. The printed 2 × 2 mm2 films were attached on a sample holder with a tilting angle of 45° or 90° to the horizontal plane. The distance between the sample holder and the fog outlet of the humidifier was 20 mm [19]. A small container was placed under the surface and on a digital balance (resolution: 0.1 mg) to collect and measure the weight of water droplets harvested by the surface. The water collection of each surface was conducted for 30 min.

Quantitative measurements were obtained by comparing the weight of water collected per unit time and unit area [44,45]. **Figure 11a** shows the quantitative measurements of the water collection efficiency as a function of the surface type and the tilt angle. At 90° tilt angle, among the four tested surfaces, the S_{cf} surface showed the lowest water collection efficiency (21 mg cm^{-2} min^{-1}). The S_{pf} surface reached the water collection efficiency of approximately 37 mg cm^{-2} min^{-1} within a 30 min cycle. The S_{pf} surface collects more water than the S_{cf} surface because the hydrophobic nature of the S_{pf} surface allows droplets to roll down into the water collecting container more efficiently instead of adhesion and evaporation. By adding microgroove surface structures, the grooved polymer surface S_{pg} is more efficient (50 mg cm^{-2} min^{-1}) than the flat polymer surface S_{pf}. This can be attributed to the Laplace pressure gradient due to groove geometry, which assists in the directional droplet removal, with comparatively lower sliding resistance. A sharp increase in the collection efficiency of 84 mg cm^{-2} min^{-1} was observed for S_{cg}. Compared with S_{cf}, S_{pf}, and S_{pg} surfaces, the increase in fog harvesting ability of S_{cg} surface was approximately 68%, 127%, and 300%, respectively. A similar trend was observed when the samples were tilted at 45°. A comparison between our work and the data found in previous studies with wettability contrast is listed in **Fig. 11b**. It can be seen that our work demonstrated the most significant enhancement in both the water collection efficiency and efficiency increase compared to the flat polymer surface counterpart. It implies that the AS-TPP process developed in our

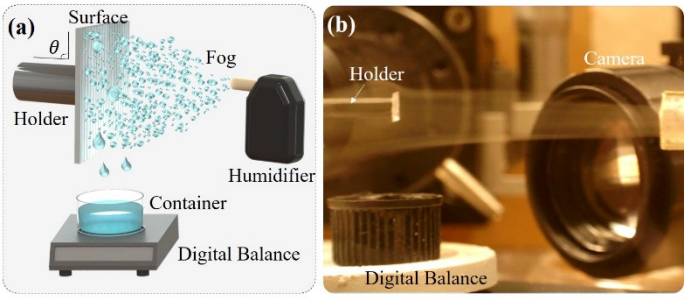

Fig. 10 Fog harvesting and water collection experimental setup: (a) schematic diagram; **(b)** a commercial humidifier is used to produce fog with the substrate placed on a holder, and the collected water in the container is measured by a digital balance.

work is highly effective in fabricating anisotropic multimaterial components with micro-scale surface structures and simultaneously high material contrast.

The in-situ observation and high-resolution camera recording were performed to understand the fog harvesting process and analyze the fundamental mechanism behind the fog harvesting behaviors of the four sample surfaces. **Figure 12** shows snapshot images of all four samples at 90° inclination angle during the fog harvesting experiments (t = 1, 3, and 360s). Due to the high surface energy of the hydrophilic composite material that enables water absorption, the water droplets on the flat composite surface, S_{cf} were captured within 1s and then immediately spread over to form thin films with non-uniform sizes, as shown in **Fig. 12a**. In contrast, fewer water droplets were captured initially on the S_{pf} surface, which is composed purely of the hydrophobic polymer, and after a few seconds, spherical droplets were observed, as shown in **Fig. 12b**. Due to the lower surface energy, the nucleation speed on the hydrophobic polymer surface S_{pf} (3s nucleation time) is slower than that on the hydrophilic composite surface S_{cf} (1s nucleation time).

The captured tiny droplets gradually merged with the nearby droplets on the polymer sample surface S_{pf}, and once size increased beyond a certain threshold, the droplets rolled off at the bottom edge.

Compared to the flat sample surfaces S_{cf} and S_{pf}, the droplet growth and rolling mechanisms on the grooved surfaces S_{pg} and S_{cg} were significantly different. Initially, the water droplets on the grooved surfaces were arranged along the microgroove direction. Once the droplets grew larger than the groove width, they merged with nearby droplets with a slight oval shape on the S_{pg} surface. Laplace pressure gradient due to the microgrooves provided low sliding resistance, and the aggregated smaller droplets rolled to the bottom edge, forming larger aggregates, as shown in **Fig. 12c**. On the grooved composite surface S_{cg}, droplets grew and merged on the pure polymer plateau region, same as observed on the grooved polymer surface S_{pg}. However, due to the surface energy gradient, the merged droplets on the S_{cg} surface roll into the composite microgroove areas after contacting the border of the grooves. Finally, driven by the Laplace pressure gradient, continuous downward transportation of collected droplets took place, making space for new droplets to get collected, as shown in **Fig. 12d**. This continuous droplet collection and drainage capability of the S_{cg} surface allow it to possess the highest water collection efficiency compared to all other surfaces.

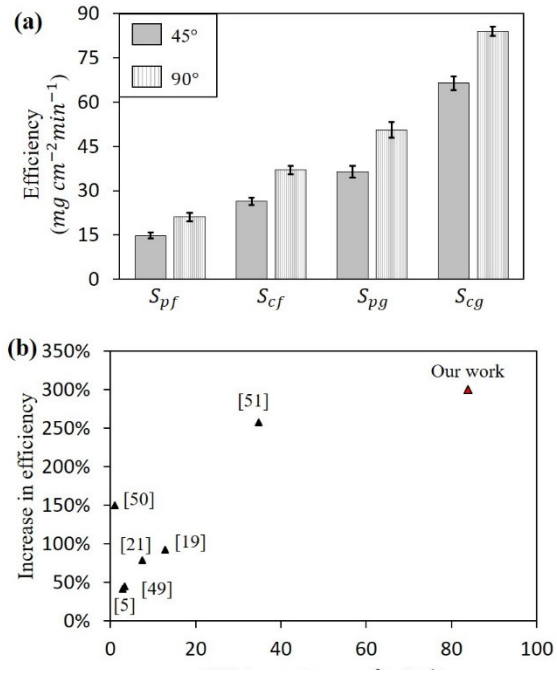

Fig. 11 Fog harvesting efficiency data: (a) water collection efficiency of different samples at 45° and 90° tilting angles. Results are presented as the mean ± standard deviation (replication n = 3); **(b)** plot comparing the increase in water collection efficiency reported in the literature (black) and our work (red).

5. Conclusion

This study demonstrated the design and fabrication of bioinspired anisotropic multimaterial surfaces using the novel Acoustic Streaming-assisted Two-Photon Polymerization (AS-TPP) process. Four surfaces with different topology and chemical composition designs were systematically fabricated. The printed geometry and chemical composition were characterized using SEM imaging and EDS analysis. The measured geometry dimensions in all sample surfaces agreed well with the designed geometries. Furthermore, the EDS analysis of the samples clearly showed the anisotropic distribution of iron oxide nanoparticles and the particle concentration within the microgrooves.

To demonstrate the effectiveness of the AS-TPP technology on the manufacturing of multi-material anisotropic structures and their potential applications, the anisotropic wettability and fog harvesting capability of the AS-TPP printed structures were investigated. It was found that the anisotropic multimaterial structures could effectively increase the wetting

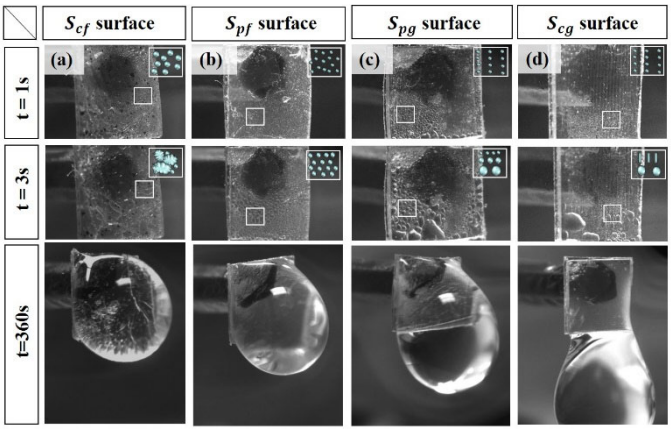

Fig. 12 Images of the fog harvesting process at different times (t = 1, 3, 360 s) for: (a) flat composite surface (S_{cf}); **(b)** flat pure polymer surface (S_{pf}); **(c)** grooved pure polymer surface (S_{pg}); **(d)** grooved composite surface (S_{cg}).

anisotropy (i.e., contact angle difference along two orthogonal directions) up to 43 ° without any further need for chemical treatment or surface modification. Besides, the proposed surface can effectively work as a highly efficient fog collecting surface and significantly enhance the water collection efficiency due to the energy and Laplace pressure gradient. Compared with the flat hydrophilic composite surface counterpart, an enhancement of >300% in water collection efficiency was observed on the grooved composite surface fabricated by the AS-TPP process.

The present work shows that anisotropic surfaces fabricated using the AS-TPP process can feature microscale surface structures and simultaneously high chemical contrast, which together result in large function anisotropies. In particular, our test case demonstrated the anisotropic wetting and high water collection efficiency of the AS-TPP printed anisotropic particle-polymer composite structures. The proposed anisotropic multimaterial structure manufacturing method is simple and does not require any additional surface treatment methods. Considering the freedom of patterning a variety of nanoparticles via acoustic field, this research can be further expanded to designing and producing multifunctional anisotropic structures for varied applications. For instance, by simply increasing the concentration of MNPs, it could be possible to achieve localized control of cell adhesion and automated cell proliferation in the desired regions and along the desired directions [51]. Future work will focus on investigating AS-TPP for manufacturing anisotropic multimaterial components with other surface structures, e.g., extending the current parallel microgroove surface structure to an island or network surface structures. Other applications will also be explored, including optic/electronic devices, cell screening and culturing, and bio-sensing.

Acknowledgments

We thank the partial financial support from National Science Foundation (Grant No. 1663399). The authors are thankful for the service from the UIC Nanotechnology Core Facility and Electron Microscopy Core. The authors also thank Lina Lichade for her help on taking the rice leaf microscopic image.

References

[1] Li H, Li A, Zhao Z, Li M, Song Y. Heterogeneous Wettability Surfaces: Principle, Construction, and Applications. Small Struct 2020;1:2000028. https://doi.org/10.1002/sstr.202000028.

[2] Tawfick S, De Volder M, Copic D, Park SJ, Oliver CR, Polsen ES, et al. Engineering of micro- and nanostructured surfaces with anisotropic geometries and properties. Adv Mater 2012;24:1628–74. https://doi.org/10.1002/adma.201103796.

[3] Autumn K, Gravish N. Gecko adhesion: Evolutionary nanotechnology. Philos Trans R Soc A Math Phys Eng Sci 2008;366:1575–90. https://doi.org/10.1098/rsta.2007.2173.

[4] Zheng Y, Gao X, Jiang L. Directional adhesion of superhydrophobic butterfly wings. Soft Matter 2007;3:178–82. https://doi.org/10.1039/b612667g.

[5] Upadhyay RK, Waghmare PR. Green preparation of copper surfaces with wettability contrast for guided fluid transport and fog harvesting application. Mater Lett 2019;246:223–6. https://doi.org/10.1016/j.matlet.2019.03.053.

[6] Lu C, Lipson RH. Interference lithography: A powerful tool for fabricating periodic structures. Laser Photonics Rev 2010;4:568–80. https://doi.org/10.1002/lpor.200810061.

[7] Parness A, Soto D, Esparza N, Gravish N, Wilkinson M, Autumn K, et al. A microfabricated wedge-shaped adhesive array displaying gecko-like dynamic adhesion, directionality and long lifetime. J R Soc Interface 2009;6:1223–32. https://doi.org/10.1098/rsif.2009.0048.

[8] Lu Y, Yu L, Zhang Z, Wu S, Li G, Wu P, et al. Biomimetic surfaces with anisotropic sliding wetting by energy-modulation femtosecond laser irradiation for enhanced water collection. RSC Adv 2017;7:11170–9. https://doi.org/10.1039/c6ra28174e.

[9] Huang Z, Geyer N, Werner P, De Boor J, Gösele U. Metal-assisted chemical etching of silicon: A review. Adv Mater 2011;23:285–308. https://doi.org/10.1002/adma.201001784.

[10] Wang Y, Shang L, Chen G, Sun L, Zhang X, Zhao Y. Bioinspired structural color patch with anisotropic surface adhesion. Sci Adv 2020;6. https://doi.org/10.1126/sciadv.aax8258.

[11] Lee JH, Ro HW, Huang R, Lemaillet P, Germer TA, Soles CL, et al. Anisotropic, hierarchical surface patterns via surface wrinkling of nanopatterned polymer films. Nano Lett 2012;12:5995–9. https://doi.org/10.1021/nl303512d.

[12] Zhao H, Park SJ, Solomon BR, Kim S, Soto D, Paxson AT, et al. Synthetic Butterfly Scale Surfaces with Compliance-Tailored Anisotropic Drop Adhesion. Adv Mater 2019;31:1–6. https://doi.org/10.1002/adma.201807686.

[13] Korkmaz S, Kariper IA. Fog harvesting against water shortage. Environ Chem Lett 2020;18:361–75. https://doi.org/10.1007/s10311-019-00950-5.

[14] Schnell G, Jagow C, Springer A, Frank M, Seitz H. Time-dependent anisotropic wetting behavior of deterministic structures of different strut widths on Ti6Al4V. Metals (Basel) 2019;9. https://doi.org/10.3390/met9090938.

[15] Parker AR, Lawrence CR. Water capture by a desert beetle. Nature 2001;414:33–4.

[16] Garimella MM, Koppu S, Kadlaskar SS, Pillutla V, Abhijeet, Choi W. Difference in growth and coalescing patterns of droplets on bi-philic surfaces with varying spatial distribution. J Colloid Interface Sci 2017;505:1065–73. https://doi.org/10.1016/j.jcis.2017.06.099.

[17] Kostal E, Stroj S, Kasemann S, Matylitsky V, Domke M. Fabrication of Biomimetic Fog-Collecting Superhydrophilic-Superhydrophobic Surface Micropatterns Using Femtosecond Lasers. Langmuir 2018;34:2933–41. https://doi.org/10.1021/acs.langmuir.7b03699.

[18] Zhong Y, Jacobi AM, Georgiadis JG. Effects of surface chemistry and groove geometry on wetting characteristics and droplet motion of water condensate on surfaces with rectangular microgrooves. Int J Heat Mass Transf 2013;57:629–41. https://doi.org/10.1016/j.ijheatmasstransfer.2012.10.056.

[19] Yang X, Song J, Liu J, Liu X, Jin Z. A Twice Electrochemical-Etching Method to Fabricate Superhydrophobic-Superhydrophilic Patterns for Biomimetic Fog Harvest. Sci Rep 2017;7:1–12. https://doi.org/10.1038/s41598-017-09108-1.

[20] Li H, Lai Y, Huang J, Tang Y, Yang L, Chen Z, et al. Multifunctional wettability patterns prepared by laser processing on superhydrophobic TiO2 nanostructured surfaces. J Mater Chem B 2015;3:342–7. https://doi.org/10.1039/c4tb01814a.

[21] Lin J, Tan X, Shi T, Tang Z, Liao G. Leaf Vein-Inspired Hierarchical Wedge-Shaped Tracks on Flexible Substrate for Enhanced Directional Water Collection. ACS Appl Mater Interfaces 2018;10:44815–24. https://doi.org/10.1021/acsami.8b13012.

[22] Liu W, Fan P, Cai M, Luo X, Chen C, Pan R, et al. An integrative bioinspired venation network with ultra-contrasting wettability for large-scale strongly self-driven and efficient water collection. Nanoscale 2019;11:8940–9. https://doi.org/10.1039/c8nr10003a.

[23] Mao M, He J, Li X, Zhang B, Lei Q, Liu Y, et al. The emerging frontiers and applications of high-resolution 3D printing. Micromachines 2017;8:1–20. https://doi.org/10.3390/mi8040113.

[24] Ge P, Wang S, Zhang J, Yang B. Micro-/nanostructures meet anisotropic wetting: From preparation methods to applications. Mater Horizons 2020;7:2566–95. https://doi.org/10.1039/d0mh00768d.

[25] Zhang L, Wu J, Hedhili MN, Yang X, Wang P. Inkjet printing for direct micropatterning of a superhydrophobic surface: Toward biomimetic fog harvesting surfaces. J Mater Chem A 2015;3:2844–52. https://doi.org/10.1039/c4ta05862c.

[26] Geng H, Bai H, Fan Y, Wang S, Ba T, Yu C, et al. Unidirectional water delivery on a superhydrophilic surface with two-dimensional asymmetrical wettability barriers. Mater Horizons 2018;5:303–8. https://doi.org/10.1039/c7mh01138e.

[27] Li P, Cao M, Bai H, Zhao T, Ning Y, Wang X, et al. Unidirectional Liquid Manipulation Via an Integrated Mesh with Orthogonal Anisotropic Slippery Tracks. Adv Funct Mater 2019;29:1–7. https://doi.org/10.1002/adfm.201904446.

[28] Chi J, Zhang X, Wang Y, Shao C, Shang L, Zhao Y. Bio-inspired wettability patterns for biomedical applications. Mater Horizons 2021;8:124–44. https://doi.org/10.1039/d0mh01293a.

[29] Jafari R, Cloutier C, Allahdini A, Momen G. Recent progress and challenges with 3D printing of patterned hydrophobic and superhydrophobic surfaces. Int J Adv Manuf Technol 2019;103:1225–38. https://doi.org/10.1007/s00170-019-03630-4.

[30] Liu X, Gu H, Ding H, Du X, He Z, Sun L, et al. Programmable Liquid Adhesion on Bio-Inspired Re-Entrant Structures. Small 2019;15:1–8. https://doi.org/10.1002/smll.201902360.

[31] Lichade KM, Jiang Y, Pan Y. Hierarchical Nano/Micro-Structured Surfaces with High Surface Area/Volume Ratios. J Manuf Sci Eng Trans ASME 2021;143:1–11. https://doi.org/10.1115/1.4049850.

[32] Lakhotia SR, Mukhopadhyay M, Kumari P. Iron oxide (FeO) nanoparticles embedded thin-film nanocomposite nanofiltration (NF) membrane for water treatment. Sep Purif Technol 2019;211:98–107. https://doi.org/10.1016/j.seppur.2018.09.034.

[33] Lichade KM, Pan Y. Acoustic Field-Assisted Two-Photon Polymerization Process. J Manuf Sci Eng 2021;143:1–7. https://doi.org/10.1115/1.4050759.

[34] Lichade KM, Hu S, Pan Y. Two-Photon Polymerization of Anisotropic Composites using Acoustic Streaming. Manuf Lett 2021. https://doi.org/10.1016/j.mfglet.2021.09.001.

[35] Chen M, Cai F, Wang C, Wang Z, Meng L, Li F, et al. Observation of Metal Nanoparticles for Acoustic Manipulation. Adv Sci 2017;4. https://doi.org/10.1002/advs.201600447.

[36] Nørgaard T, Dacke M. Fog-basking behaviour and water collection efficiency in Namib Desert Darkling beetles. Front Zool 2010;7:1–8. https://doi.org/10.1186/1742-9994-7-23.

[37] Florio LA. Numerical investigation of particle trapping in various groove configurations in straight and bent flow channels. Simulation 2020;96:679–99. https://doi.org/10.1177/0037549720922600.

[38] Kang SM, Lee C, Kim HN, Lee BJ, Lee JE, Kwak MK, et al. Directional oil sliding surfaces with hierarchical anisotropic groove microstructures. Adv Mater 2013;25:5756–61. https://doi.org/10.1002/adma.201302083.

[39] Cioffi M, Moretti M, Manbachi A, Chung BG, Khademhosseini A, Dubini G. A computational and experimental study inside microfluidic systems: The role of shear stress and flow recirculation in cell docking. Biomed Microdevices 2010;12:619–26. https://doi.org/10.1007/s10544-010-9414-5.

[40] Manbachi A, Shrivastava S, Cioffi M, Chung BG, Moretti M, Demirci U, et al. Microcirculation within grooved substrates regulates cell positioning and cell docking inside microfluidic channels. Lab Chip 2008;8:747–54. https://doi.org/10.1039/b718212k.

[41] Fan Y, Xu F, Huang G, Lu TJ, Xing W. Single neuron capture and axonal development in three-dimensional microscale hydrogels. Lab Chip 2012;12:4724–31. https://doi.org/10.1039/c2lc40312a.

[42] Jothi Prakash CG, Prasanth R. Approaches to design a surface with tunable wettability: a review on surface properties. J Mater Sci 2021;56:108–35. https://doi.org/10.1007/s10853-020-05116-1.

[43] Janson IA, Kong YP, Putnam AJ. Nanotopographic substrates of poly (methyl methacrylate) do not strongly influence the osteogenic phenotype of mesenchymal stem cells in vitro. PLoS One 2014;9. https://doi.org/10.1371/journal.pone.0090719.

[44] Park JK, Kim S. Three-dimensionally structured flexible fog harvesting surfaces inspired by Namib desert beetles. Micromachines 2019;10. https://doi.org/10.3390/mi10030201.

[45] Bai H, Wang L, Ju J, Sun R, Zheng Y, Jiang L. Efficient water collection on integrative bioinspired surfaces with star-shaped wettability patterns. Adv Mater 2014;26:5025–30. https://doi.org/10.1002/adma.201400262.

[46] Mahmood A, Chen L, Chen S, Chen C, Yu Y, Weng D, et al. Nature-inspired design of conical array for continuous and efficient fog collection application. Colloids Interface Sci Commun 2020;37:100283. https://doi.org/10.1016/j.colcom.2020.100283.

[47] Yao Y, Machado C, Jiang Y, Feldman E, Aizenberg J, Park K-C. Liquid Collection on Welwitschia-Inspired Wavy Surfaces n.d.

[48] Kyong Kim N, Hee Kang D, Eom H, Wook Kang H. Biomimetic fog harvesting surface by photo-induced micro-patterning of zinc-oxide silver hierarchical nanostructures. Appl Surf Sci 2019;470:161–7. https://doi.org/10.1016/j.apsusc.2018.11.132.

[49] Sharma V, Yiannacou K, Karjalainen M, Lahtonen K, Valden M, Sariola V. Large-scale efficient water harvesting using bioinspired micro-patterned copper oxide nanoneedle surfaces and guided droplet transport. Nanoscale Adv 2019;1:4025–40. https://doi.org/10.1039/c9na00405j.

[50] Zhou H, Jing X, Li S, Guo Z. Near-bulge oil meniscus-induced migration and condensation of droplets for water collection: Energy saving, generalization and recyclability. Chem Eng J 2021;417:129215. https://doi.org/10.1016/j.cej.2021.129215.

[51] Webb K, Hlady V, Tresco PA. Relative importance of surface wettability and charged functional groups on NIH 3T3 fibroblast attachment, spreading, and cytoskeletal organization. J Biomed Mater Res 1998;41:422–30. https://doi.org/10.1002/(SICI)1097-4636(19980905)41:3<422::AID-JBM12>3.0.CO;2-K.

[52] Zhang S, Huang J, Chen Z, Yang S, Lai Y. Liquid mobility on superwettable surfaces for applications in energy and the environment. J Mater Chem A 2019;7:38–63. https://doi.org/10.1039/c8ta09403a.